Energy & Environmental Science

Accepted Manuscript

ROYAL SOCIETY OF CHEMISTRY

www.rsc.org/ees

Energy & Environmental Science

PAPER

Light-guided Electrodeposition of Non-Noble Catalyst Patterns for Photoelectrochemical Hydrogen Evolution

Received 00th January 20xx,
Accepted 00th January 20xx

DOI: 10.1039/x0xx00000x

www.rsc.org/

Sung Yul Lim,[a] Yang-Rae Kim,[a] Kyungyeon Ha,[b,c] Jong-Kwon Lee,[c] Jae Gyeong Lee,[a] Woohyuk Jang,[a] Jin-Young Lee,[a] Je Hyun Bae,[a] and Taek Dong Chung[*,a,d]

Hydrogen is in the lime light as a carbon-free alternative energy source due to its high energy conversion efficiency. Solar-driven water splitting is one of the most promising methods for renewable hydrogen production. However, commercialization of a photoelectrochemical hydrogen production system remains a great challenge. One of the emerging concern is the development of inexpensive and transparent catalyst not to obstruct the light pathways to semiconductor electrode. Here we report a non-noble metal electrocatalyst for hydrogen evolution, Ni-Mo, which is directly patterned on amorphous Si (a-Si) by light-guided spatially selective electrodeposition without consecutive photolithography process. A light pattern is illuminated onto the a-Si using a digital micromirror device to commence the photoelectrochemical deposition. The catalyst patterned by the proposed method not only admits sufficient light to the a-Si but also enables long distance carrier transport along the inversion layer, as previously observed in crystalline Si (c-Si) photocathodes. This new electrodeposition method enables mask-free patterning on the a-Si and is expected to expedite a lower cost, more efficient, and self-biasing integrated photoelectrochemical water-splitting device.

Broader context

Hydrogen production using water splitting has attracted enormous attention as a renewable energy source. However, much effort is still required for practical commercialization. For utilizing photoelectrochemical (PEC) system, one of the greatest concern is the catalyst design not to obstruct the light absorption to underlying semiconductor. What we chose in this study is spatially separated Ni-Mo, a well-known non-noble catalyst for hydrogen evolution. Exploiting the photoconductive nature of hydrogenated amorphous Si (a-Si), we carried out direct electrodeposition of patterned Ni-Mo by illuminating light using a digital micromirror device. This process was completed in a single step without any mask. Such patterned Ni-Mo photocathode have bare surface, through which light can transmit. In addition, long-distance lateral electron transport is found between the adjacent NiMo patterns on a-Si photocathode. Our approach enables the inherent current density and photovoltage, which expected to be applied for a-Si based heterojunction photocathode for higher efficiency.

Introduction

Unremitting effort has continued since the pioneering work of Fujishima and Honda in 1972,[1] to produce storable chemical fuels, particularly hydrogen, more efficiently by photoelectrochemical (PEC) reactions. Recently, significant advances in stability and efficiency were achieved by the metal-insulator-semiconductor (MIS)-based photoelectrode configuration.[2-7] Photo-generated electrons at the semiconductor penetrate the insulator and transfer to the metal layer, which should serve as an electrocatalyst for hydrogen evolution. However, MIS-based photoelectrodes, in practice, are facing difficulties of unsated photoelectrochemical performance and high cost. To date, considerable efforts for MIS photoelectrodes system have been made in developing "transparent catalysts" to permit the light transmission while maintaining the sufficient amount of catalyst loaded, which can be classified into four approaches.[8-11] The first approach involves the placement of transparent conducting oxide (TCO) beneath the catalyst/insulator/semiconductor photoelectrodes and illumination from the back side through TCO.[12] This permits a wider range of materials to be used, including opaque catalysts, but the high expense of TCO must be addressed.[13] The second approach is to seek new electrocatalytic materials to replace noble metals. Reportedly, thin layers (monolayers to a few nanometers) of Pt do not severely interrupt light transmission and can exhibit sufficient catalytic performance in acidic condition.[14-16] The third approach is to massively load non-precious metal catalysts onto a large semiconductor surface

[a] Department of Chemistry, Seoul National University, Seoul 08826, Korea. email: tdchung@snu.ac.kr; Tel: +82.2.880.4362
[b] Department of Mechanical and Aerospace Engineering, Seoul National University, Seoul 08826, Korea.
[c] Global Frontier Center for Multiscale Energy Systems, Seoul National University, Seoul 08826, Korea.
[d] Advanced Institutes of Convergence Technology (AICT), Suwon-Si, Gyeonggi-do 16229, Korea.

†Electronic Supplementary Information (ESI) available: Complete materials and methods, Fig. S1-S16. See DOI: 10.1039/x0xx00000x

area, despite the poor saturation current density.[17-19] The fourth approach is to utilize molecular catalysts. Due to the perfect transparency and ideal for chemical study of catalyst operation mechanism, much efforts have been made to design and synthesize new molecular electrocatalysts for hydrogen evolution (HER).[20-23] Although several molecular HER catalysts show high turnover frequency, stability issue especially in aqueous conditions is still challenging.[8,24] The final approach employs patterned catalysts that leave bare surfaces between neighbouring electrodes for optical transmission. Such a surface is exposed to the solution as well as light. With an MIS photoelectrode based on crystalline Si (c-Si), this strategy has proven to be promising by recent works showing that patterned Pt/Ti catalysts can bring about substantial enhancement in PEC activity for the HER.[6,7]

Various methods have been proposed to fabricate patterned electrodes.[25-30] Most are template-assisted techniques based on typical photolithography, posing inherent limitations in terms of complexity, cost, and scalability. Electrodeposition is a relatively simple method that enables cost-effective formation of metal and semiconductor nanostructures with scalability.[31-33] Furthermore, the surface characteristics as well as the amount of electrodeposited materials can be varied through the nucleation process and growth rate by adjusting the magnitude and duration of the applied voltage or current pulses.[34,35] However, there is a critical prerequisite for spatial-selective electrodeposition to be a successful alternative to photolithography in fabricating patterned MIS system, viz. a pre-patterned conductive electrode on which the catalytic electrodes are electrodeposited is required.

Amorphous Si (a-Si) is a photoconductive material with a short ambipolar diffusion length of about 115 nm.[36-39] It is a renowned light absorber with a direct band gap of 1.7 eV, significantly overlapping with the solar spectrum.[40-42] Owing to the photoconductive nature of a-Si, electrochemical reduction could selectively occur where illuminated.[43-46] Herein, we demonstrate light-guided, spatially selective, and direct electrodeposition of Ni-Mo, non-noble electrocatalyst for HER,[5,18,19] on the a-Si substrate. The desired pattern is constructed as a bitmap image file by computer, and light with the same pattern is illuminated onto the a-Si to induce a virtual electrode by local, photogenerated electrons. Electrochemical reduction by potential pulses generates a correspondingly patterned MIS junction. Interestingly, the MIS junction based on a-Si in this work shows abnormally long lateral electron transport, reminiscent of what was previously observed at the photocathodes based on c-Si.[6,7] This effectively relieves not only the interruption of light transmission, but also the dependence of HER on the distance between neighboring non-noble catalysts.

Results and discussion

In this system, a-Si was deposited on highly doped n-type Si(100) by plasma-enhanced chemical vapour deposition. To overcome the inherent low photo-induced voltage, we prepared a-Si with a buried p-i-n junction for high open circuit voltage.[5] Protective layer on Si-based photoelectrode, on which electrodeposition is to occur, is essential because of the vulnerability of Si surface in aqueous electrochemical conditions. For this purpose, we formed chemical oxide, denoted by SiO_x herein, by immersing the a-Si photoelectrodes in mixed solutions of H_2SO_4 and H_2O_2 after complete removal of the native oxide. The chemical oxide is thin enough to transfer photogenerated charge carriers by tunneling and also serves as an insulating layer to prevent direct contact of the electrolyte solution with the Si-based photoelectrode surface over a wide range of pHs and potentials.[47,48] In addition, the lower defect density of the chemical oxide than the native oxide, i.e., fewer recombination sites, contributes to higher PEC activity[47,48]

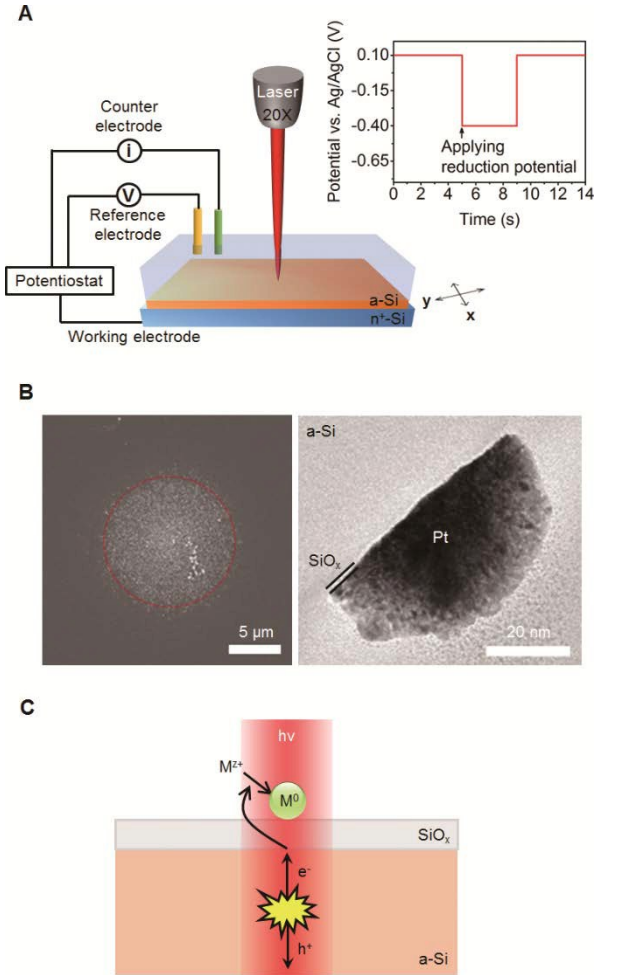

Fig. 1 Scheme of light-guided spatially selective electrodeposition on a-Si under 632.8 nm laser illumination. (A) Schematic view of experimental setup and potential profile for Pt electrodeposition. (B) Top view SEM image of electrodeposited Pt nanoparticles (red circle: illuminated area with laser) and cross-sectional HRTEM image of single Pt nanoparticle/SiO_x/a-Si interface. The thickness of SiO_x layer was 1 to 2 nm. (C) Schematic illustration of the mechanism for light-guided electrodeposition.

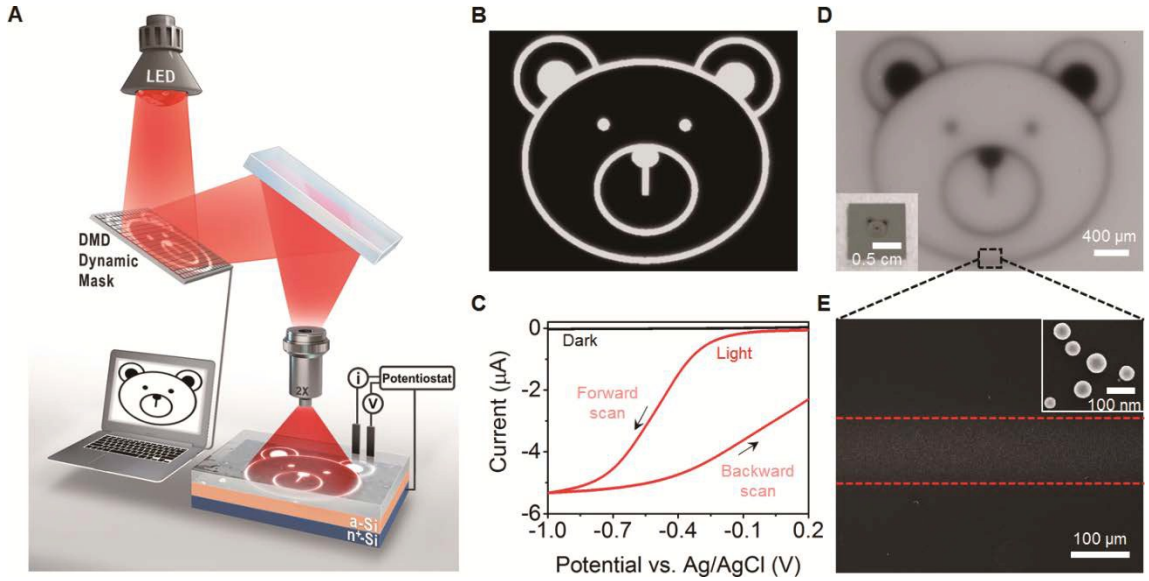

Fig. 2 LED-based electro-patterning on large area using DMD dynamic mask system. (A) Schematic view of DMD display system for electro-patterning. (B) Image of photomask generated by 625 nm LED and DMD display. (C) Cyclic voltammogram recorded during Pt electrodeposition under shaped illumination (shown in B). (D) Optical image of electrodeposited Pt pattern that corresponds to the photomask loaded onto DMD. Inset shows the photograph of the pattern formed on a-Si substrate. (E) SEM image of the selected area marked in D. Pt nanoparticles consist of a line, as shown in the inset image. Dotted lines in red indicate the illuminated area.

In order to demonstrate a proof-of-concept of the light-guided electrodeposition technique using the photoconductivity of a-Si, we patterned one of representative electrocatalysts, Pt. As illustrated in Figure 1A, a typical three electrode configuration enables the electrochemistry, and a 632.8 nm He/Ne laser is focused on the substrate through the aqueous electrolyte solution that contains Pt precursor ions. Under illumination, an electric potential pulse for Pt electrodeposition is applied via the highly doped Si wafers underneath the a-Si. The applied potential leads to Pt nanoparticles that appear at the illuminated sites (Fig. 1B). The electrochemically generated Pt nanoparticles are stable and adhesive to the oxide surface, as confirmed by the negligible loss in the optical images taken before and after several washing processes (Fig. S1, ESI†). The HRTEM image in Figure 1B shows the polycrystalline Pt nanoparticles on a-Si. The chemical oxide film formed by wet chemical process herein was about 1 to 2 nm thick. This result indicates that the electrons produced by focused light on the photoconductive a-Si, are used for faradaic reduction which takes place nowhere but the illuminated spot (Fig. 1C). This is not surprising in that ambipolar diffusion length in a-Si is less than 115 nm. Making use of this phenomenon, we can enable mask-free light-guided direct electrodeposition on a-Si.

For rapid patterning on larger areas, we replaced the laser illumination module with a red LED (625 nm) combined with a digital micromirror device (DMD) to create the optical image corresponding to that drawn in the computer (Fig. 2A). As shown in Figure 2B, the resulting light images loaded to the DMD board were focused on the a-Si surface through a 2× objective lens. The maximum size of the light images produced by DMD was 13 mm × 10 mm and the minimum line width was around 100 μm. Cyclic voltammetry was conducted under the focused LED light with the pattern of a bear face (Fig. 2B) onto the a-Si substrate under the same electrolyte conditions as Figure 1A. Since the current during the reverse scan was greater than that during the initial forward scan, we can see that the a-Si surface is irreversibly modified with conductive material that can act as an electrode (Fig. 2C). Pt in this case is electrodeposited during the initial negative potential scan. Compared with the voltammogram under illumination, almost negligible current and no electrodeposition of Pt was observed at the dark conditions (Fig. 2C). At a constant potential of -0.4 V (vs. Ag/AgCl) for 180 s, Pt nanoparticles are deposited in the same pattern as the light image created by DMD (Fig. 2D). Current-time curve recorded at -0.4 V (vs. Ag/AgCl) during the Pt electrodeposition is shown in Figure S2 (ESI†).

To look into the role of light in this system, we recorded the total charge passed throughout the electrodeposition as a function of the diameter of the light images (Figs. S3A and S3B, ESI†). The total charge passed has a linear relationship with the illuminated areas that coincides with the areas of the actually deposited Pt dots. In addition, the total charge linearly increases with the number of dots generated by DMD (Fig. S3C, ESI†). These results reveal that the light-guided electrodeposition reproducibly produces the pattern that exactly corresponds to the loaded images on DMD, and the deposition reaction takes place uniformly over the illumination site. The ultimate resolution of this patterning method is about 100 μm when using a 2× objective lens, as shown in Figure 2E. As confirmed by Figure 1B, the spatial resolution of our patterning method is limited by the size of the illuminated light spot, ~10 μm diameter, made by a laser through a 20× objective lens.

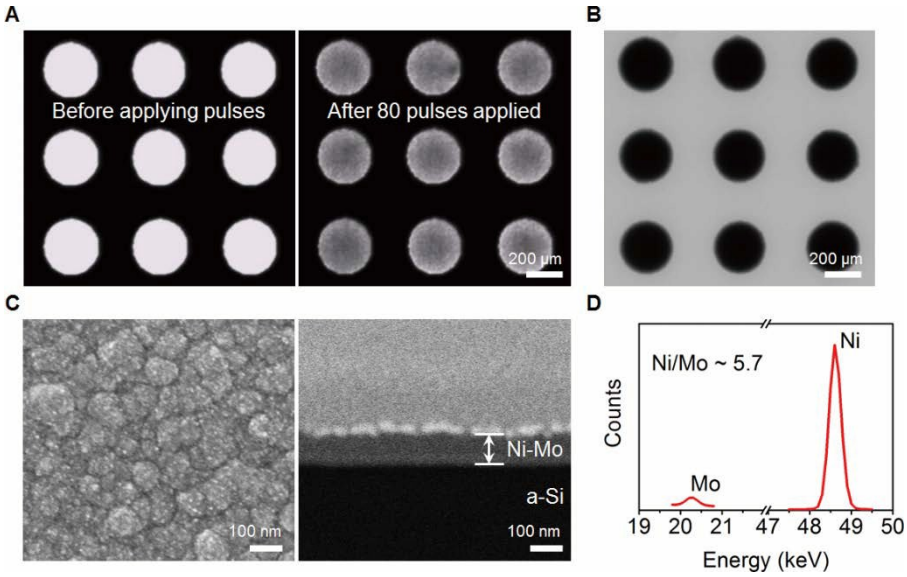

Fig. 3 Spatially selective electrodeposition of non-noble HER catalyst, Ni-Mo, at SiO_x/a-Si and XRF results. (A) Change in image during the Ni-Mo electrodeposition under dot-patterned illumination. (B) Optical image of dot-patterned Ni-Mo catalyst electrodeposited from the photomask shown in A, generated by DMD. (C) Top view, and cross-sectional SEM image of the Ni-Mo film. Cross-sectional image was taken in EsB mode of the SEM device. (D) XRF spectra of Ni and Mo for quantitative analysis of Ni/Mo ratio.

The proposed patterning method can be applied to electrodeposition of Ni-Mo, a well-known non-noble catalyst for the hydrogen evolution reaction (HER) on a-Si substrate. Reduction potential pulses at -0.9 V (vs. Ag/AgCl) were applied for 10 s, followed by open circuit potentials (+0.35 V vs. Ag/AgCl) for 5 s. Precursor ions are replenished during the period of the resting potential so that the potential pulse technique can yield a more dense and uniform Ni-Mo film. As shown in the images taken during the electrodeposition of Ni-Mo (Fig. 3A), the illuminated sites are blackened by the deposited Ni-Mo as a result of 80 reduction pulses (see the video clip). After the programmed potential bias is applied, a greenish film with a dot shape appears on the a-Si substrate (Fig. 3B). Consistent with the results of Pt electrodeposition, Ni-Mo patterning reflects the reliability and expandability of the proposed method. Figure 3C shows the scanning electron microscopy (SEM) images of the top and cross section of the Ni-Mo catalysts on the a-Si. The deposited Ni-Mo is a roughened conformal film containing cracks and pinholes. This morphology originates from the hydrogen bubbles that appear during the deposition process referring to the reported literature.[18] The Ni-Mo films are about 150 nm thick for 80 reduction pulses applied. The Ni/Mo ratio calculated from X-ray fluorescence (XRF) spectroscopy is about 5.7, which is similar to previously reported results (Fig. 3D).[18,19]

As illustrated in the schematic energy band diagram of Figure 4A, the p-i-n type of a-Si has a band structure similar to that of the p-type,[49] indicating that it can function as a photo-generated electron supplier for solar-driven electrochemical reduction of protons. Electrons from excitons created by light absorption migrate to the semiconductor/electrolyte interface following an electric field across the MIS junction, and transfer through SiO_x to the Ni-Mo catalysts where faradaic reduction takes place. In Figure 4B, we see that the current density from the linear sweep voltammetry (LSV) remarkably increases in the presence of Ni-Mo compared with the bare a-Si surface. The influence of the number of patterned Ni-Mo dots on the current for hydrogen evolution has an implication in how PEC HER occurs using photo-induced electro-patterned Ni-Mo. As

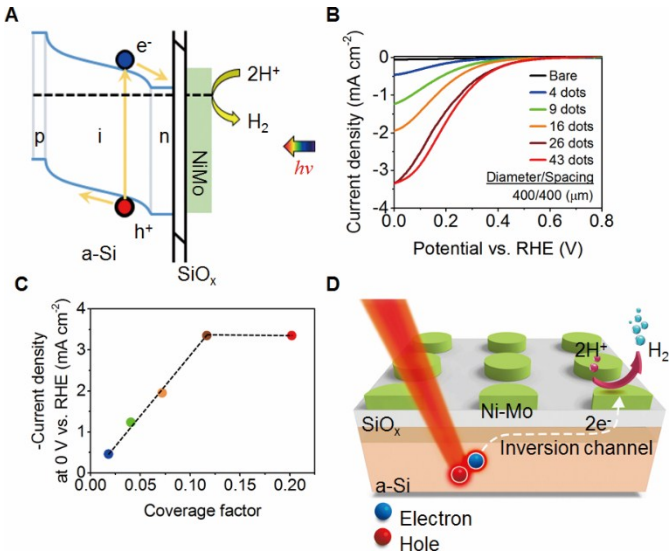

Fig. 4 PEC performance at patterned Ni-Mo/SiO_x/a-Si photocathode. (A) Schematic energy band diagram of Ni-Mo/SiO_x/a-Si junction for PEC HER. (B) LSVs for HER at the Ni-Mo pattern/SiO_x/a-Si junction photocathode in deaerated 0.2 M aqueous potassium hydrogen phthalate buffer (pH 4.5) with 0.2 M K_2SO_4 as a function of the number of Ni-Mo dots, in which individual dot areas are constant, 400 μm in diameters, and neighboring dots are equally spaced by 400 μm. So more dots means larger net area of Ni-Mo array that are at the center of the electrode. (C) The correlation between the Ni-Mo coverage factor and the current density at 0 V vs. RHE. The colors of circles correspond to those of the curves in (B). Coverage factor is the ratio of the Ni-Mo array area to the entire area of photoelectrode, which is 0.28 cm^2. (D) Schematic illustration of HER operation mechanism at Ni-Mo pattern/SiO_x/a-Si photocathode.

reported in the previous work performed with Pt/Ti/SiO_2/*p*-Si(100) photocathode,[7] current densities for all voltammograms should be saturated at sufficiently high overpotential to similar limiting current irrespective of the number of Ni-Mo dots. It is because HER should take place at bare photoelectrode surface as well as catalyst illuminated if the spillover-assisted hydrogen evolution governs the photoelectrode system.[7] However, the current density at 0 V vs. reversible hydrogen electrode (RHE) in the proposed system increases in proportional to the number of Ni-Mo dots, indicating augment of surface coverage by Ni-Mo catalyst for constant exposed photoelectrode area. Negligible current was observed without illumination (Fig. S4, ESI†). This result corroborates the role of patterned Ni-Mo as a catalyst, which lets photo-generated electrons drain out effectively for light-driven electrochemical HER. As shown in Figure 4C, the current density at 0 V (vs. RHE) is saturated at the 60% (about 0.12) of the highest coverage tested (about 0.20) where diameter and spacing are 400 and 400 μm, respectively. Keeping in mind negligible catalytic activity at bare a-Si surface covered with SiO_x for HER, the photogenerated electrons must travel much longer distances through the a-Si to reach the catalytic sites than in bulk a-Si. This observation indirectly supports the long-lateral electron diffusion along a-Si edge. Based on these results, Figure 4D illustrates the electron transport through the Ni-Mo pattern/SiO_x/a-Si photocathode for hydrogen generation.

To demonstrate the effects of long-distance lateral electron transport in a-Si and transfer to the semiconductor/electrolyte interface, we conducted experiments of 'remote electrodeposition'. As shown in Figure 5A, a line of Au was electrodeposited in the same way where was apart by 1600 μm from the center of the pre-patterned Pt line, which was also exposed to the electrolyte containing Au precursors. As shown in Figure 5B and Figure S5 (ESI†), Au nanoparticles grow on the bare a-Si where it is illuminated, as well as on pre-patterned Pt nanoparticles where it is dark. The cathodic current for Au deposition is much higher in the presence of the pre-patterned Pt. Interestingly, a little hump is found at ~4 s in the *i-t* curve of Au electrodeposition with pre-patterned Pt, while it does not appear on the bare a-Si surface without Pt (Fig. 5C). The current hump is usually observed due to overlapping diffusion fields in electrochemical systems in which nanoparticles grow.[31] Au nanoparticle was electrodeposited nowhere else under dark conditions. Referring to the study at metal/self-assembled monolayers/metal system,[50-52] we can assume that once a metal seed is formed on SiO_x/a-Si by tunneling, charge transfer to it would become more facile. Higher density of states (DOS) due to the presence of the metal seed reportedly contributes to more probable electron transfer through the thin insulating layer.[50-52] As illustrated in Figure 5D, faradaic reduction can occur at the metal structures as well as at the illuminated region of a-Si, indicating the long-distance transport through the a-Si. Because of this phenomenon, single-shot patterning on a large area of a-Si using the LED-DMD

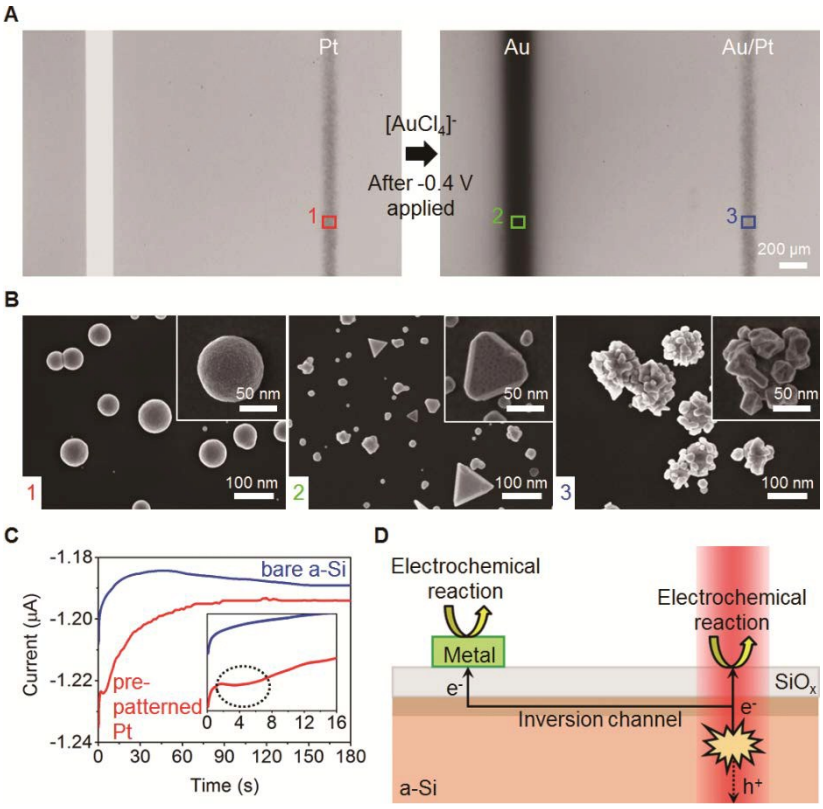

Fig. 5 Remote electrodeposition to investigate long-distance lateral electron transport in a-Si. (A) Optical images of light-guided Au electro-patterning 1.6 mm from the pre-patterned Pt line feature. (B) SEM images at each area marked on panel A. (C) Current-time (*i-t*) curves recorded during the Au electrodeposition in the absence and presence of pre-patterned Pt. Inset shows a little hump (marked by the black dotted circle) at the initial stage. (D) Schematic illustration of long-distance lateral electron transport along inversion layer in a-Si.

combination is preferred to continuously writing with a focused laser beam. The electrochemical growth continues where it was previously scanned but is currently in the dark so that the electrodeposited lines are hardly controlled (Fig. S6, ESI†).

To further examine the dependence of PEC HER activity on lateral electron transport, we measured the local photocurrents as the focused 530 nm LED light was displaced from the pre-patterned Ni-Mo (Fig. S7, ESI†). The photocurrent decreases with increasing the distance from the Ni-Mo catalyst, presumably attributed to electron-phonon scattering and electron-hole recombination. However, as previously observed in the remote electrodeposition experiments, the photocurrent can flow even when the light source is illuminated at much longer (1 mm) than the ambipolar diffusion length of a-Si (115 nm) from the metallic collector, Ni-Mo. This long-distance travel of electron in a-Si may be unfavorable for the operation mechanism of spatially selective electrodeposition induced by local illumination. However, the patterning resolution is not seriously dependent on lateral electron transport because electron transfer to the electrolyte solutions in dark region occurs not through the bare a-Si surface, but through the MIS junction only, as shown in Figs. 4B and 5. Esposito *et al*. and Ji *et al*.[6,7] suggested that diffusion along unexpectedly long distance in crystalline Si (c-Si) is ascribed to the inversion layer beneath the oxide layer. The proposed Ni-Mo/SiO_x/a-Si photoelectrode for HER also exhibits the light-induced transition in the capacitance-voltage curve at +0.35 V (vs. RHE), which is similar to the behavior observed for c-Si (Fig. S8, ESI†).[7] In line with the previous reports on c-Si, we postulate that protons at a negative bias may play a critical role in electron transport at silicon/electrolyte interfaces because protons can diffuse in the thin oxide layer by virtue of intimate chemical attraction with the Si surface and oxide layer.[7,53-55]

Despite the lateral transport of photo-generated electrons through the inversion channel, the long distance does not favor current density due to electron-phonon scattering and recombination. On the other hand, too short channel length between the patterned catalysts suffers from light transmission to the underlying a-Si, which results in the decrease of current density (Fig. 6B). Thus, it is important to compromise both factors and find the proper spacing among the Ni-Mo patterns. Prior to the systematic investigation of the spacing effect, we determined the optimal amount of catalyst electrodeposited for each spacing by comparing the current density at 0 V (vs. RHE). Narrower spacing requires fewer pulses for Ni-Mo electrodeposition (Fig. S9 and Fig. S10, ESI†). As the spacing among the catalysts gets narrower, less amount of Ni-Mo catalyst for individual dot is needed to reach the maximal current (Fig. S11, ESI†).

From the linear sweep voltammograms in Figure 6B, the best spacing for 400 μm diameter Ni-Mo dots was determined to be 130 μm for the hydrogen evolution. Spacing wider than 130 μm leads to lower current density. This can be understood by taking into account of limited lateral electron transport along inversion layer, which is deterred by electron-phonon scattering and recombination. On the other hand, the current density also

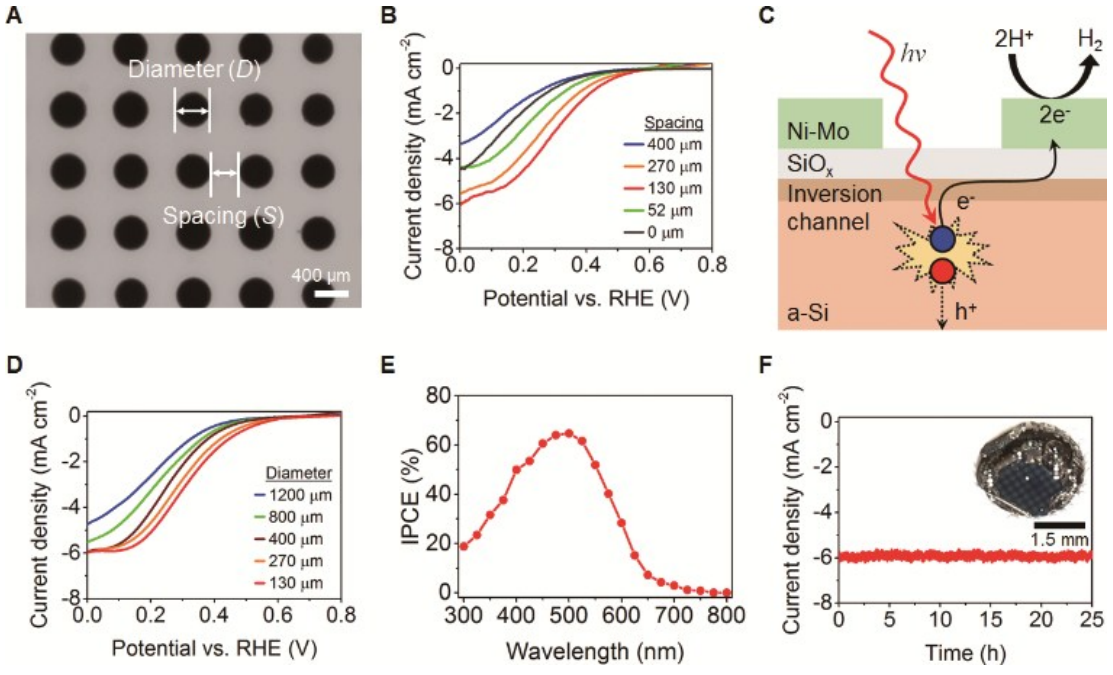

Fig. 6 HER performance of Ni-Mo pattern/SiO_x/a-Si photocathodes with patterns of different diameters and spacing under simulated AM 1.5 illumination in deaerated pH 4.5 buffer. (A) Optical image of Ni-Mo pattern/SiO_x/a-Si photocathode. (B) Linear sweep voltammograms for various spacing of Ni-Mo dots of constant diameter, 400 μm. The 0 μm of spacing indicates the photocathode of non-patterned Ni-Mo/SiO_x/a-Si. (C) Schematic illustration of electron transport through Ni-Mo pattern/SiO_x/a-Si junction and transfer for proton reduction. (D) Linear sweep voltammograms for a variety of catalyst diameters with constant spacing of 130 μm. (E) IPCE measured using monochromatic light from a Xenon arc lamp and applied bias of 0 V (vs. RHE). (F) Stability test by chronoamperometry at a constant 0 V (vs. RHE) for 25 h. Both IPCE and stability measurements were conducted at *D*/*S* of 130/130 μm Ni-Mo pattern/SiOx/a-Si photocathode. Inset shows the photograph of hydrogen bubbles formed at photoelectrodes during stability measurements.

drops for spacings shorter than 130 μm, presumably because of significant optical loss caused by absorption and/or scattering by the Ni-Mo catalysts. This is confirmed by the total reflectance (TR) from Ni-Mo pattern/SiO_x/a-Si in the wavelength ranging from 300 to 800 nm as a function of spacing among Ni-Mo dots (Fig. S12, ESI†). TR keeps decreasing as the catalysts get closer until the spacing is as short as 130 μm. For more closely patterned Ni-Mo dots including fully covered with Ni-Mo, TR spectra depend on the wavelength. As the spacing is shortened further to be 52 and 0 μm, TR increases at shorter wavelength than 600 nm, probably due to reflection by Ni-Mo, while it continues to decrease in longer wavelength region. Therefore, TR let us estimate the coverage of the Ni-Mo catalyst on SiO_x/a-Si for maximal light absorption. In addition, we confirm the same trend of spacing effects on PEC HER at the Ni-Mo dots of 130 μm in diameter (Fig. S13, ESI†).

Varying the diameter of the uniformly spaced Ni-Mo dots provides further information on the effect of the catalyst pattern on the PEC activity. The linear sweep voltammograms in Figure 6D indicate that the onset potentials (at J = -0.1 mA cm^{-2}) and V_{MPP} (MPP, maximum power point) shift positively as the dot becomes smaller, resulting in higher applied-bias photon-to-current efficiency (ABPE, ABPE was calculated assuming an ideal counter electrode, Fig. S14, ESI†). The current density at 0 V (vs. RHE) continues to increase as the diameter decreases from 1200 to 800 μm, and reaches a plateau at less than 800 μm. The best ABPE in the proposed system is 1.06% for a diameter/spacing (D/S) of 130/130 μm (Fig. S15, ESI†). The principle that underlies this phenomenon is unclear yet. One of the reason may be that the edge of the catalyst is located near the bare photoelectrode surface.[7,56] Further research to collect direct evidence is underway. The current density of -6 mA cm^{-2} (at 0 V vs. RHE) and the V_{OC} of 620 mV are close to the inherent performance in Pt/planar a-Si photocathodes,[49] indicating that the sufficient non-noble catalyst loading with the negligible optical losses by the catalysts. The ABPE of this system, which is lower than that of photocathodes based on c-Si, results from the low incident photon-to-current conversion efficiency (IPCE) at short wavelengths and near band edge region (Fig. 6E). How we calculated IPCE is given in Fig. S16 (ESI†). Such behavior was previously reported in the external quantum efficiency (EQE) of a-Si solar cells.[57] The low IPCE at wavelengths shorter than 400 nm is attributed to the recombination at defect sites caused by the B-doped region of p-type a-Si.[57] Figure 6F shows that the proposed system does not suffer from degradation for approximately one day at 0 V (vs. RHE) and the faradaic efficiency at 0 V (vs. RHE) was 98.4% after 60 minutes reaction under simulated AM 1.5 illumination.

Conclusions

In this study, we have demonstrated a solar-driven photocathode for the water-splitting device fabricated by light-guided Ni-Mo electrodeposition. The computer-aided virtual photomask by a digital micromirror device (DMD) enables direct patterning based on photo-induced electrodeposition on a-Si for flexibility, scalability, and high throughput with high yield compared to the typical photolithography. By virtue of this new method, Ni-Mo, which is a well-known non-precious electrocatalyst for hydrogen evolution, was directly patterned onto the a-Si photoelectrode. The direct patterning of non-noble electrocatalysts for the PEC HER in this work has great potential for further improvement. The patterned MIS junction composed of low cost materials can enhance the PEC activity for HER by integrating additional light trapping structures, high-quality protective layers that have proper band alignment with respect to the hydrogen evolution potentials for reduced electron extinction,[3,6,58] optimization of inversion channels to deploy protons, and finer tuning of pattern design and microstructures of catalysts. We expect that the current work will lead to important advances toward efficient, self-biasing, integrated PEC water splitting for practical commercialization. In addition, this technique have great potential for wide range of applications requiring patterned substrates such as biosensors, electronic devices, and the photoelectrode systems related to the energy conversion reaction, e.g. CO_2 reduction and oxygen evolution reaction.

Experimental

Preparation of a-Si photocathodes

Amorphous Si photoelectrodes were fabricated using highly doped n-type Si(100) wafers (0.001–0.003 Ω cm). Si wafers were cleaned using a standard Radio Corporation of American (RCA) cleaning procedure,[59] and then transferred to a plasma-enhanced chemical vapor deposition (PECVD) chamber for a-Si deposition. Triple layers of p-type a-Si:H (20 nm), intrinsic a-Si:H (500 nm), and n-type a-Si:H (100 nm) were deposited sequentially. The a-Si deposited wafers were diced into 1 cm × 1 cm. The native oxides on a-Si were removed by immersion of the electrodes in 1% HF solutions and then transferred to piranha solutions (1:3 H_2O_2:H_2SO_4) for 60 s to grow the chemical oxide. The electrodes were rinsed with deionized water (resistivity of 18.2 MΩ cm at 25 ˚C) and dried with a N_2 gun. These electrodes were stored in a vacuum desiccator in the dark before use.

Light-guided spatially selective electrodeposition

Spatially selective electrodeposition was conducted using two different light sources. To demonstrate the idea, we used a laser (632.8 nm He/Ne laser, LASOS Lasertechnik GmbH) as part of a home-built micro-Raman system (Dongwoo Optron Co., Ltd.). The laser intensity was 1 mW. For generation of optical pattern images, a homemade digital micromirror device display module (Uninanotech) equipped with a 625 nm LED (Mightex, PLS-0625-030-S) was installed on the BX43 Olympus upright microscope. Under focused light illumination, potential pulses were generated by a CHI 440 electrochemical workstation. All electrochemical experiments were carried out using a standard three-electrode configuration in a homemade Teflon cell. For wiring the working electrode to the a-Si photocathode, the Si

backside was scratched, and oxide was removed using a few drops of 1% HF solution only on the scratched area of the Si backside. After rinsing with deionized water, the electrodes were dried by blowing N_2 (99.9%) gas, and wired with Al conductive tape smeared with a Ga-In eutectic. Pt wire and Ag/AgCl (3 M NaCl, Bioanalytical System, Inc.) were employed as counter and reference electrodes, respectively. The electrodeposition bath was purged with high-purity N_2 gas (99.9%) before applying reduction potentials. Na_2PtCl_6 (1 mM) and $NaAuCl_4$ (1 mM) containing 0.5 M Na_2SO_4 (adjusted to pH 3 with 0.5 M H_2SO_4) as a supporting electrolyte were used for light-guided spatially selective electrodeposition of Pt and Au, respectively. The Ni-Mo electrodeposition bath contained 130 mM $Ni(SO_3NH_2)$, 50 mM H_3BO_3, and 2 mM $NaMoO_4$ (the pH was adjusted to 4.0). All electrolyte solutions for the electrochemistry experiments were prepared with deionized water (resistivity of 18.2 MΩ cm at 25 ˚C).

PEC measurements

A 150 W Xenon arc lamp equipped with a 1.5 G filter was used as the solar-simulating light source. The light intensity was calibrated to 100 mW cm^{-2} with a radiometer (Solar light, PMA-2100) and a pyranometer (PMA-2144). For all electrochemical measurements, the reference electrode and counter electrode was Ag/AgCl (3 M NaCl, Bioanalytical System, Inc.) and Pt wire, respectively. The potentials versus Ag/AgCl reference electrode (0.209 V vs. NHE) were converted to reversible hydrogen electrode (RHE) potential using the $E(H^+/H_2)$ = -0.47 V vs. Ag/AgCl, measured by commercialized RHE electrode (ALS Co., Ltd). Considering the pH of 4.5, the potentials of -0.47 V was almost consistent with the value predicted by the Nernst equation. LSVs were performed using a CHI 440 electrochemical workstation in deaerated 0.2 M potassium hydrogen phthalate solution with 0.2 M K_2SO_4 as supporting electrolyte (adjusted to pH 4.5 using 2 M KOH) at a scan rate of 10 mV s^{-1}. The electrolyte was continuously bubbled with N_2 gas. The RHE potential was invariant before and after the LSV measurements, determined by measuring open circuit potential (OCP) versus Ag/AgCl electrode. While recording the LSVs, the solution was circulated at a rate of 5 mL s^{-1} using a peristaltic pump. Before the LSV experiments, cyclic voltammetry (CV) was conducted until the voltammograms were stabilized between +0.4 V and -0.5 V (vs. Ag/AgCl). The influence of oxygen gas evolved at the Pt counter electrode in the long-term stability test at 0 V (vs. RHE) was prevented by immersion of the Pt counter electrode in a separate chamber connected with glass frits, while the reference electrode was immersed in the main chamber. In addition, the oxygen in the electrolyte was purged with the high-purity H_2 gas (99.9%) to maintain a constant RHE potential. The potential shift was negligible after the 25 hours photoelectrolysis (±5 mV, OCP measured by RHE vs. Ag/AgCl). Capacitance-voltage (*C*-*V*) measurements were conducted by a Gamry Reference 600 (Gamry Instruments, Warminster, PA) with 100 Hz AC frequency under AM 1.5 illumination and dark conditions. Incident-photon-to-current efficiency was performed using a 150 W Xenon arc lamp combined with a monochromator. The light intensity of the monochromatic wavelength was measured using a radiometer and pyranometer. Faradaic efficiency was given by: $2n_{H2}F/Q$, where n_{H2} is the total amount of produced hydrogen (mol) analyzed by gas chromatography (YL6100GC, Young Lin Instrument) with our sealed home-built quartz photoelectrochemical cell under N_2 gas environment. F is the Faraday constant and Q is the total amount of charge (C) passed. It was obtained by integrating the current that flew at 0 V (vs. RHE) for 1 hour.

Acknowledgements

This research was supported by the Nano.Material Technology Development Program (No. 2011-0030268), the Global Frontier R&D Program on Center for Multiscale Energy System (No. 2012M3A6A7055873), and by the National Research Foundation (No. 2015R1A2A1A13001897), funded by the Ministry of Science, ICT & Future Planning, Korea.

References

1 A. Fujishima and K. Honda, *Nature*, 1972, **238**, 37-38.
2 Y. W. Chen, J. D. Prange, S. Duehnen, Y. Park, M. Gunji, C. E. D. Chidsey and P. C. McIntyre, *Nat. Mater.*, 2011, **10**, 539-544.
3 S. Hu, M. R. Shaner, J. A. Beardslee, M. Lichterman, B. S. Brunschwig and N. S. Lewis, *Science*, 2014, **344**, 1005-1009.
4 J. Yang, K. Walczak, E. Anzenberg, F. M. Toma, G. Yuan, J. Beeman, A. Schwartzberg, Y. Lin, M. Hettick, A. Javey, J. W. Ager, J. Yano, H. Frei and I. D. Sharp, *J. Am. Chem. Soc.*, 2014, **136**, 6191-6194.
5 Y. Lin, C. Battaglia, M. Boccard, M. Hettick, Z. Yu, C. Ballif, J. W. Ager and A. Javey, *Nano Lett.*, 2013, **13**, 5615-5618.
6 L. Ji, M. D. McDaniel, S. Wang, A. B. Posadas, X. Li, H. Huang, J. C. Lee, A. A. Demkov, A. J. Bard, J. G. Ekerdt and E. T. Yu, *Nat. Nanotechnol.*, 2015, **10**, 84-90.
7 D. V. Esposito, I. Levin, T. P. Moffat and A. A. Talin, *Nat. Mater.*, 2013, **12**, 562-568.
8 J. R. McKone, N. S. Lewis and H. B. Gray, *Chem. Mater.*, 2014, **26**, 407-414.
9 T. J. Jacobsson, V. Fjallstrom, M. Edoff and T. Edvinsson, *Energy Environ. Sci.*, 2014, **7**, 2056-2070.
10 Z. Chen, S. Ye, A. R. Wilson, Y.-C. Ha and B. J. Wiley, *Energy Environ. Sci.*, 2014, **7**, 1461-1467.
11 W. D. Chemelewski, H.-C. Lee, J.-F. Lin, A. J. Bard and C. B. Mullins, *J. Am. Chem. Soc.*, 2014, **136**, 2843-2850.
12 J. J. H. Pijpers, M. T. Winkler, Y. Surendranath, T. Buonassisi and D. G. Nocera, *Proc. Natl. Acad. Sci. U. S. A.*, 2011, **108**, 10056-10061.
13 M. Aparicio, A. Jitianu, L. C. Klein, *Sol-Gel Processing for Conventional and Alternative Energy*, page 286; Springer New York Heidelberg Dordrecht London, 2012.
14 M. G. Walter, E. L. Warren, J. R. McKone, S. W. Boettcher, Q. Mi, E. A. Santori and N. S. Lewis, *Chem. Rev.*, 2010, **110**, 6446-6473.
15 A. Heller, D. E. Aspnes, J. D. Porter, T. T. Sheng and R. G. Vadimsky, *J. Phys. Chem.*, 1985, **89**, 4444-4452.
16 J. Kye, M. Shin, B. Lim, J.-W. Jang, I. Oh and S. Hwang, *ACS Nano*, 2013, **7**, 6017-6023.
17 P. Dai, J. Xie, M. T. Mayer, X. Yang, J. Zhan and D. Wang, *Angew. Chem. Int. Ed.*, 2013, **52**, 11119-11123.

18 J. R. McKone, E. L. Warren, M. J. Bierman, S. W. Boettcher, B. S. Brunschwig, N. S. Lewis and H. B. Gray, *Energy Environ. Sci.*, 2011, **4**, 3573-3583.
19 E. L. Warren, J. R. McKone, H. A. Atwater, H. B. Gray and N. S. Lewis, *Energy Environ. Sci.*, 2012, **5**, 9653-9661.
20 X. L. Hu, B. M. Cossairt, B. S. Brunschwig, N. S. Lewis and J. C. Peters, *Chem*. *Commun*., 2005, 4723-4725.
21 M. L. Helm, M. P. Stewart, R. M. Bullock, M. R. DuBois and D. L. DuBois, *Science*, 2011, **333**, 863-866.
22 S. C. Marinescu, J. R. Winkler and H. B. Gray, *Proc. Natl. Acad. Sci. U. S. A.*, 2012, **109**, 15127-15131.
23 M. O'Hagan, M.-H. Ho, J. Y. Yang, A. M. Appel, M. R. DuBois, S. Raugei, W. J. Shaw, D. L. DuBois and R. M. Bullock, *J. Am. Chem. Soc.*, 2012, **134**, 19409-19424.
24 C. Madden, M. D. Vaughn, I. Diez-Perez, K. A. Brown, P. W. King, D. Gust, A. L. Moore and T. A. Moore, *J. Am. Chem. Soc.*, 2012, **134**, 1577-1582.
25 H. Kim, J. Kim, H. Yang, J. Suh, T. Kim, B. Han, S. Kim, D. S. Kim, P. V. Pikhitsa and M. Choi, *Nat*. *Nanotechnol*., 2006, **1**, 117-121.
26 Z. H. Nie and E. Kumacheva, *Nat*. *Mater*., 2008, 7, 277-290.
27 E. J. Menke, M. A. Thompson, C. Xiang, L. C. Yang and R. M. Penner, *Nat*. *Mater*., 2006, **5**, 914-919.
28 A. Sinitskii and J. M. Tour, *J. Am. Chem. Soc.*, 2010, **132**, 14730-14732.
29 B. Hatton, L. Mishchenko, S. Davis, K. H. Sandhage and J. Aizenberg, *Proc. Natl. Acad. Sci. U. S. A.*, 2010, **107**, 10354-10359.
30 T. S. Mentzel, D. D. Wanger, N. Ray, B. J. Walker, D. Strasfeld, M. G. Bawendi and M. A. Kastner, *Nano Lett*., 2012, **12**, 4404-4408.
31 P. V. Dudin, P. R. Unwin and J. V. Macpherson, *J. Phys*. *Chem*. *C*, 2010, **114**, 13241-13248.
32 S. Manne, P. K. Hansma, J. Massie, V. B. Elings and A. A. Gewirth, *Science*, 1991, **251**, 183-186.
33 D. M. Kolb, R. Ullmann and T. Will, *Science*, 1997, **275**, 1097-1099.
34 P. V. Dudin, M. E. Snowden, J. V. Macpherson and P. R. Unwin, *ACS Nano*, 2011, **5**, 10017-10025.
35 Y. Lu, Z. Tu and L. A. Archer, *Nat*. *Mater*., 2014, 13, 961-969.
36 R. C. Hayward, D. A. Saville and I. A. Aksay, *Nature*, 2000, **404**, 56-59.
37 P. Y. Chiou, A. T. Ohta and M. C. Wu, *Nature*, 2005, **436**, 370-372.
38 H. Hwang, H. Chon, J. Choo and J.-K. Park, *Anal*. *Chem*., 2010, **82**, 7603-7610.
39 S. Ota, S. Wang, Y. Wang, X. Yin and X. Zhang, *Nano Lett*., 2013, **13**, 2766-2770.
40 D. J. Harrison, G. S. Calabrese, A. J. Ricco, J. Dresner and M. S. Wrighton, *J. Am. Chem. Soc.*, 1983, **105**, 4212-4219.
41 G. S. Calabrese, M. S. Lin, J. Dresner and M. S. Wrighton, *J. Am. Chem. Soc.*, 1982, **104**, 2412-2417.
42 C. M. Gronet, N. S. Lewis, G. W. Cogan, J. F. Gibbons, G. R. Moddel and H. Wiesmann, *J. Electrochem*. *Soc*., 1984, **131**, 2873-2880.
43 R. H. Micheels, *Appl*. *Phys*. *Lett*., 1981, **39**, 418.
44 T. L. Rose, *Appl*. *Phys*. *Lett*., 1983, **42**, 193.
45 T. Inoue, A. Fujishima and K. Honda, *J. Electrochem*. *Soc*., 1980, **127**, 1582-1588.
46 S.-H. Huang, H.-J. Hsueh and Y.-L. Jiang, Biomicrofluidics, 2011, **5**, 034109.
47 T. Hattori, K. Watanabe, M. Ohashi, M. Matsuda and M. Yasutake, *Appl*. *Surf*. *Sci*., 1996, **102**, 86-89.
48 K. Saito, M. Matsuda, M. Yasutake and T. Hattori, *Jpn*. *J*. *Appl*. *Phys*., 1995, **34**, L609-L611.
49 M. Matsumura, Y. Sakai, S. Sugahara, Y. Nakato and H. Tsubomura, *Sol*. *Energy Mater*., 1986, **13**, 57-64.
50 .-N. Chazalviel and P. Allongue, *J. Am. Chem. Soc.*, 2011, **133**, 762-764.
51 G. P. Kissling, D. O. Miles and D. J. Fermin, *Phys. Chem. Chem. Phys.*, 2011, **13**, 21175-21185.
52 C. R. Bradbury, J. Zhao and D. J. Fermin, *J. Phys. Chem. C*, 2008, **112**, 10153-10160.
53 J.-Y. Lee, J. G. Lee, S.-H. Lee, M. Seo, L. Piao, J. H. Bae, S. Y. Lim, Y. J. Park and T. D. Chung, *Nat*. *Commun*., 2013, **4**, 2766.
54 M. T. Kelly, J. K. M. Chun and A. B. Bocarsly, *J. Phys*. *Chem*. *B*, 1997, **101**, 2702-2708.
55 J. Velmurugan, D. Zhan and M. V. Mirkin, *Nat*. *Chem*., 2010, **2**, 498-502.
56 A. Barkschat, H. Tributsch and J. K. Dohrmann, *Sol*. *Energy Mater*. *Sol*. *Cells*, 2003, **80**, 391-403.
57 S. Thiyagu, Z. W. Pei and M. S. Jhong, *Nanoscale Res*. *Lett*., 2012, **7**, 1-6.
58 B. Seger, T. Pedersen, A. B. Laursen, P. C. K. Vesborg, O. Hansen, and I. Chorkendorff, *J. Am. Chem. Soc.*, 2013, **135**, 1057-1064.
59 W. Kern and D. A. Puotinen, *RCA Rev*., 1970, **31**, 187-206.

Table of contents

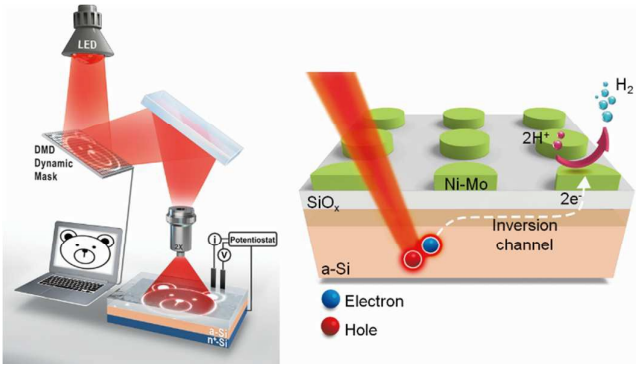

For photoelectrochemical hydrogen production, non-noble catalyst is directly patterned onto the photocathodes with light-guided electrodeposition technique.